

Exploiting the Final Component of Generator Architectures for AI-Generated Image Detection

Yanzhu Liu

Institute for Infocomm Research,
A*STAR, Singapore
liu_yanzhu@a-star.edu.sg

Yuexuan Wang

Institute for Infocomm Research,
A*STAR, Singapore
wang_yuexuan@a-star.edu.sg

Xiao Liu

Institute for Infocomm Research,
A*STAR, Singapore
liu_xiao@a-star.edu.sg

Mondal Soumik

Institute for Infocomm Research,
A*STAR, Singapore
soumik_mondal@a-star.edu.sg

Abstract

With the rapid proliferation of powerful image generators, accurate detection of AI-generated images has become essential for maintaining a trustworthy online environment. However, existing deepfake detectors often generalize poorly to images produced by unseen generators. Notably, despite being trained under vastly different paradigms, such as diffusion or autoregressive modeling, many modern image generators share common final architectural components that serve as the last stage for converting intermediate representations into images. Motivated by this insight, we propose to “contaminate” real images using the generator’s final component and train a detector to distinguish them from the original real images. We further introduce a taxonomy based on generators’ final components and categorize 21 widely used generators accordingly, enabling a comprehensive investigation of our method’s generalization capability. Using only 100 samples from each of three representative categories, our detector—fine-tuned on the DINOv3 backbone—achieves an average accuracy of 98.83% across 22 testing sets from unseen generators.

1. Introduction

“Last in Line, yet First to Reveal.”

— Inspired by Sherlock Holmes

When examining objects like a careful detective, the last touch often reveals the most, having overwritten the layers of history beneath it. Similarly, given an image and the task of determining whether it is real or AI-generated, it is crucial to examine the distinctive traces left by the generator.

Contemporary image generators are no longer monolithic; rather, they comprise multiple modular components operating in stages. This raises a natural and important question: does the last component, which serves as the final step in producing the image, leave identifiable evidence that can be exploited for detection? Our intuition is that, regardless of the generation paradigm—diffusion-based [13], autoregressive [27], or otherwise—there inevitably exists a concluding step that transforms intermediate representations into pixels, serving as the generator’s “final touch.”

We approach this question from the perspective of architecture. To clarify, the generation **architecture** refers to network components and how they are interconnected. A network **component** is a functional block composed of multiple neural layers, such as a VAE decoder, DiT transformer, or tokenizer. In contrast, most existing deepfake detection approaches focus on the generation **model**, defined as a specific set of trained weights (e.g., a pretrained network and its fine-tuned variant are considered different models). Current approaches typically generate training samples from specific generation models and design sophisticated features—such as CLIP embeddings [44], frequency-domain cues [28], multi-scale representations [19], reverse-engineered traces [16], or gradient-based signals [10]—to distinguish synthetic images from real ones. However, as new generators continue to emerge, the generalizability of existing detection approaches becomes a critical concern. When the distribution of testing data shifts significantly, these approaches often require regenerating of synthetic images from new models in order to retrain the detectors. The challenge is further amplified when users fine-tune models on custom data and keep them private.

Since real images are readily available from public

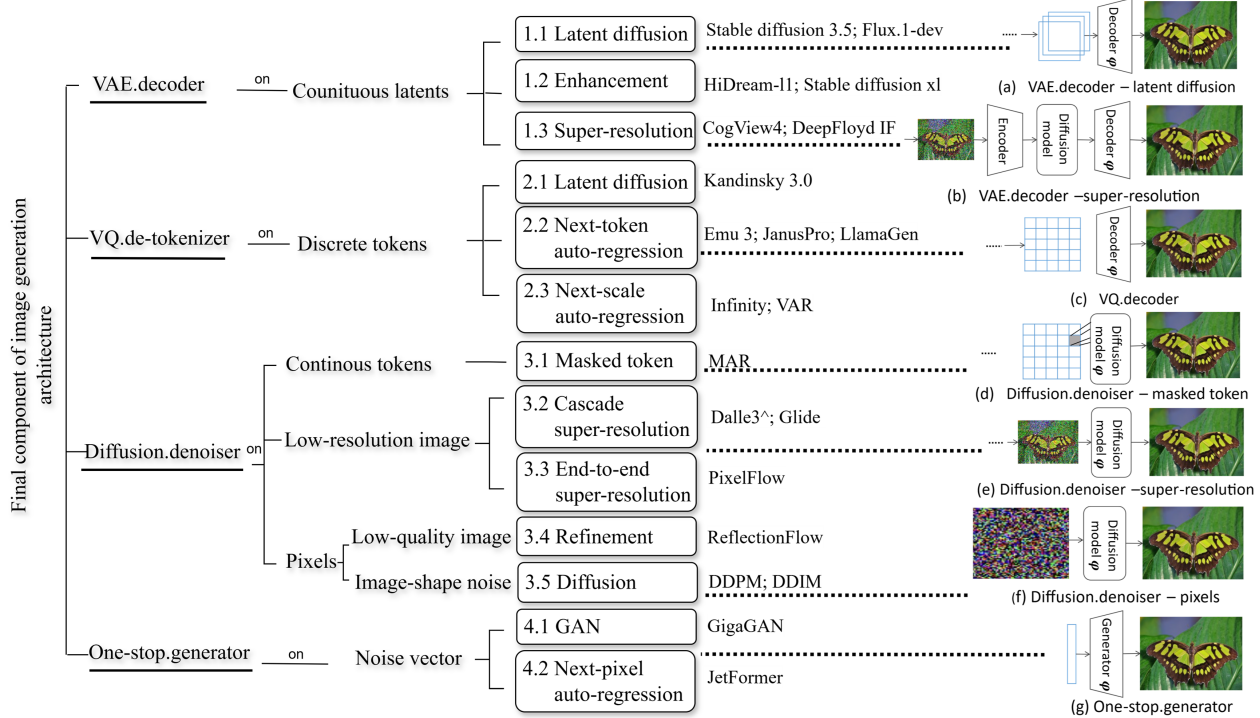


Figure 1. The proposed taxonomy of generation architectures based on final component.

datasets for image-related tasks (e.g., ImageNet, MS-COCO), we propose to “contaminate” real images with generation traces using only the generator’s final component, and subsequently train a detector to differentiate them from the original real images. Operating samples through a single component is substantially faster than executing the entire generation pipeline, particularly in diffusion models that require iterative multi-step inference. Moreover, this strategy does not necessitate the generator to be open-sourced; gray-box access to its final component suffices for implementation.

The potential generalizability of the proposed approach is motivated by three key observations: (a) many generators share similar or even identical final components; (b) relying on only a small fraction of the total parameters reduces overfitting to specific generators; (c) the contaminated images preserve identical semantic content to their real counterparts, ensuring that the detector focuses on generation artifacts rather than semantic information specific to the training set.

To comprehensively validate our hypothesis regarding the generalizability of the generator’s final component, we propose a novel taxonomy that categorizes image generators according to their final architectural component and analyze 21 widely used generators under this framework (see Fig.1). Traditionally, image generators are grouped by generation paradigm into three major categories [40]: Generative Adversarial Networks, Diffusion models, and more

recently, Autoregressive models. However, many recent generators frequently reuse common components based on their function, such as the VAE decoder, which decodes images from latent space.

From our taxonomy, we identify three representative final components—VAE decoder, super-resolution diffuser, and VQ de-tokenizer—and employ them to imprint traces onto real images as part of our approach. We observe that these components correspond to distinct trace spaces. We conduct a series of experiments to investigate: (a) whether the final component alone is sufficient to detect images generated by its corresponding full architecture; (b) whether a detector trained on one component generalizes to images generated by architectures from other categories; and (c) whether the detector remains effective on fine-tuned variants of the same component. Finally, we select 100 samples from each of the three components using K-medoids clustering, combining the 300 samples to fine-tune a detector built upon a pretrained DINOv3 [32] backbone with an appended fully-connected layer. The resulting detector achieves strong zero-shot performance across multiple challenging benchmarks.

The contributions of this study are as follows:

- We propose examining the final component of image generation architectures as a source of identifiable traces, enabling the generalizable detection.
- We introduce a novel taxonomy of text-to-image generators based on their final architectural component, which

provides insight into generalization between generators.

- By imprinting traces onto real images and training a fine-grained, region-based detector on them, our model achieves state-of-the-art zero-shot performance across generator categories and challenging benchmarks.

2. Related Work

2.1. Architecture attribution

For the deepfake detection task that this study focuses on, exploration from the perspective of generative architectures remains limited. In the related task of synthesized image attribution, which aims to identify the generator responsible for a given image, few studies have investigated attribution at the architectural level. Yang et al. [43] claimed to be the first to explore architecture attribution. They assessed GAN architectures and found that architectures leave globally consistent fingerprints, whereas model weights produce regional traces. [41] and [42] reveal that similar diffusion architectures produce similar patterns in frequency-domain features and achieve similar detection accuracies. [1] proposed a Siamese network to verify whether two images originate from the same generation architecture, while [31] applied one-class classification for open-set architecture scenarios.

2.2. Last step inversion

Few studies have examined the final step of the generation process. Laszkiewicz et al. [17] extracted features of generated images by approximating the inputs just before the final layer. The last step they focused on is a single-layer, e.g., activations, fully connected layer, or attention heads. In contrast, our study targets middle grained functional components. [39] proposed a reverse-engineering approach to map the images back to latent features. To effective inverting the decoder, they used the output from the corresponding encoder as the initialization. While related to our sample construction method for the VAE category, their work focused on model attribution and was limited to latent-based generators.

2.3. Zero-shot deepfake detection

In the zero-shot setting, the detection model is trained on samples from certain generators and applied directly to test images without fine-tuning or any prior knowledge of the generating models. Existing zero-shot methods can be broadly grouped into three categories. **Signal-level fingerprint construction** extracting low-level artifacts as detection cues, such as image gradients (LGrad [10]), pixel neighborhood differences (NPR [18]), or generator noise patterns (DIRE [16]); **CLIP-based approaches** relying solely on CLIP image features extracted from different transformer layers (UnivFD [46], RINE [23]), or incorpo-

rating text guidance using captions or prompts (e.g., “real” vs. “AI-generated”) to steer classification (DeFake [25], C2P-CLIP [44], LASTED [6]); **Robust feature design** building more resilient features, such as fusing frequency-space features (AIDE [28]) or learning multi-scale features through contrastive learning (CoDE [19]). However, none of these methods explicitly account for the influence of the generator’s architecture or components on the generated images—a gap our approach aims to address.

3. Method

We aim to investigate whether the final component leaves identifiable traces in generated images when all preceding components are omitted, and how well such traces generalize across different generation architectures. The core idea is to use real images to elicit generation signatures and train a binary classifier on them. Let the training set of real images be denoted as $\mathcal{D} = \{\mathbf{x}\}$, where each image $\mathbf{x} \in \mathbb{R}^{h \times w \times 3}$ is labeled as 1 (indicating a real image). Let $\varphi^*(\cdot) : \mathbb{S}^d \rightarrow \mathbb{R}^{h \times w \times 3}$ represent the final component of a well-trained generative model, where \mathbb{S}^d is an internal space. To simplify notation, we do not distinguish the model’s parameter set from its corresponding mapping function, e.g., φ^* denotes both the mapping function implemented by a network module and its learnable parameters. The objective function of the proposed AI-generated image detection is the standard cross-entropy on real images and reconstructed counterparts, as in Eq. 1:

$$\mathcal{L}(\theta; \mathcal{E}) := -E_{\mathbf{x} \sim p_{\mathcal{D}}} [\log(\theta(\mathbf{x}) + \log(1 - \theta(\varphi^*(\mathcal{E}(\mathbf{x}))))]] \quad (1)$$

where $\mathcal{E}(\cdot) : \mathbb{R}^{h \times w \times 3} \rightarrow \mathbb{S}^d$ is a function that maps RGB image into internal space. In generative models, φ^* is optimized from the objective of ELBO:

$$(\varphi^*, \mathcal{E}^*) = \arg \min_{\varphi, \mathcal{E}} \left(-E_{\mathbf{z} \sim q_{\mathcal{E}}(\mathbf{z}|\mathbf{x})} [\log(p_{\varphi}(\mathbf{x}|\mathbf{z}))] + D_{KL}(q_{\mathcal{E}}(\mathbf{z}|\mathbf{x}) || p(\mathbf{z})) \right) \quad (2)$$

Given a test image \mathbf{x}_t , the classifier trained with Eq. 1 outputs $\theta(\mathbf{x}_t)$, indicating whether \mathbf{x}_t is real (1) or AI-generated (0).

Property 1 *If \mathcal{E}^* is used as the mapping function \mathcal{E} in Eq. 1, then the expected detection error for images generated via φ^* is not greater than that obtained using any other mapping function \mathcal{E} , i.e., $-E_{\mathbf{x} \sim p_{\mathcal{D}}} [\log(\theta_{\mathcal{E}^*}(\mathbf{x})) - E_{\mathbf{z} \sim q_{\mathcal{E}^*}(\mathbf{z}|\mathbf{x})} [\log(1 - \theta_{\mathcal{E}^*}(\varphi^*(\mathbf{z})))]] \leq -E_{\mathbf{x} \sim p_{\mathcal{D}}} [\log(\theta_{\mathcal{E}}(\mathbf{x})) - E_{\mathbf{z} \sim q_{\mathcal{E}^*}(\mathbf{z}|\mathbf{x})} [\log(1 - \theta_{\mathcal{E}}(\varphi^*(\mathbf{z})))]]$, where $\theta_{\mathcal{E}} = \arg \min \mathcal{L}(\cdot; \mathcal{E})$ and $\theta_{\mathcal{E}^*} = \arg \min \mathcal{L}(\cdot; \mathcal{E}^*)$.*

This is an idealized property concerning global minimizers, yet it suggests that using the optimal mapping function \mathcal{E}^* , which was jointly trained with φ^* in the original generator, results in a lower expected detection error.

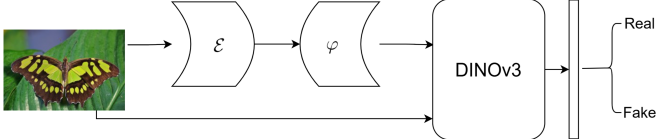


Figure 2. The proposed framework for detecting AI-generated images

Property 2 Let $\mathcal{D} = \{\mathbf{x}\}$ be real samples and $\mathcal{D}' = \{\mathbf{x}' = \varphi(\mathcal{E}(\mathbf{x})) \mid \mathbf{x} \in \mathcal{D}\}$ be constructed samples. Sampling mini-batches independently from \mathcal{D} and \mathcal{D}' , rather than using paired samples $(\mathbf{x}_i, \mathbf{x}'_i)$, yields a gradient estimator with lower variance by SGD training: $\text{Var}(\hat{\nabla}_\theta^{\text{indep}}) \leq \text{Var}(\hat{\nabla}_\theta^{\text{paired}})$

$$\hat{\nabla}_\theta^{\text{paired}} = -\frac{1}{B} \sum_{\mathbf{x} \in \mathcal{B}_t} [\nabla_\theta \log \theta(\mathbf{x}) + \nabla_\theta \log (1 - \theta(\varphi(\mathcal{E}(\mathbf{x}))))]$$

$$\hat{\nabla}_\theta^{\text{indep}} = -\frac{1}{B} \sum_{\mathbf{x} \in \mathcal{B}_t} \nabla_\theta \log \theta(\mathbf{x}) - \frac{1}{B} \sum_{\mathbf{x}' \in \mathcal{B}'_t} \nabla_\theta \log (1 - \theta(\mathbf{x}')),$$

where $\mathcal{B}_t \subseteq \mathcal{D}$ and $\mathcal{B}'_t \subseteq \mathcal{D}'$ are mini-batches of size B .

A theoretical and empirical discussion is provided in Appendix. This property suggests that independently shuffling real and constructed samples reduces the variance of the stochastic gradient, which in turn leads to more stable and faster convergence in SGD [3, 29]. Therefore, it is advantageous to construct the negative sample set \mathcal{D}' offline and sample from \mathcal{D} and \mathcal{D}' independently during SGD training.

Fig. 2 presents an overview of our method. We next detail the two key components of the objective function Eq. 1: the fake-sample construction $\varphi \circ \mathcal{E}(\cdot)$ and the detector θ . Before delving into these, we examine the final components employed by popular text-to-image generators and propose a taxonomy to systematically analyze their architectural design choices.

3.1. A Taxonomy of Generation Architectures based on Final Component

The design principles of our taxonomy, grounded in the last component $\varphi(\mathbf{z}) : \mathbb{S}^d \rightarrow \mathbb{R}^{h \times w \times 3}$, are as follows:

(1) **Position—Last**: The output of $\varphi(\mathbf{z})$ must be an image in RGB space $\mathbb{R}^{h \times w \times 3}$. We define the taxonomy categories based on the input \mathbf{z} and its input space \mathbb{S}^d .

(2) **Granularity—Middle-level**: Deep network units can be considered at four levels of granularity. The finest level refers to individual layers, such as activation or pooling layers. The second level refers to blocks composed of multiple layers that serve highly detailed functions, such as upsampler in U-Net or transformer heads. The coarsest level is the entire model. “Component” lies in the third level, representing a functional module that operates independently, such as VAE decoders or VQ de-tokenizer. This choice is motivated by two factors: many generators release pre-trained weights for such components separately, making them more

accessible without the full pipeline; and fine-grained units, like individual layers or small blocks, leave traces that are too subtle or indistinct for reliable detection.

(3) **Perspective—Implementation**. The taxonomy is based on functional implementation rather than the high-level role of the component. For example, MAR [20] performs autoregressive prediction over masked tokens but ends with a diffusion denoiser, so it is categorized as “denoiser” rather than “de-tokenizer” like other autoregressive generators. DeepFloyd IF [9] performs super-resolution in latent space and ends with a VAE decoder, placing it in the decoder category rather than denoiser like other super-resolution generators.

As illustrated in Fig. 1, we define four primary categories based on the input space \mathbb{S}^d , and further subdivide them according to what \mathbf{z} represents:

- **VAE.decoder**. In this category, the final component operates in a continuous latent space, i.e., $\mathbb{S}^d := \mathbb{R}^d$, where $d \ll h \times w \times 3$. It decodes a d -dimensional feature map or vector into the final image. As many modern generators target high-resolution outputs (e.g., 2048×2048), they often perform generation in a low-dimensional latent space for computational efficiency, relying on encoder-decoder structures for dimensionality reduction and expansion. There are three typical functional contexts in which \mathbf{z} resides: (1) **Latent diffusion**, where diffusion models operate directly in the latent space, as in the Stable Diffusion family [34] and FLUX [5]. As illustrated in Fig. 1(a), in this case, \mathbf{z} represents the denoised latent sample predicted by the diffusion model. (2) **Enhancement**, where the latent representation from the diffusion model is further refined—e.g., via GAN-based distillation—to produce a more precise \mathbf{z} before decoding, as in HiDream [4]. (3) **Latent super-resolution**, where a low-resolution image is first generated and then progressively upscaled through latent-space super-resolution stages. As shown in Fig. 1(b), the low-resolution image is noised, resized to the target size, and encoded into a latent space for diffusion processing. The resulting upscaled latent, \mathbf{z} , is then decoded to produce the final high-resolution image. Examples include CogView 4 [45] and DeepFloyd IF [9], which employ the Stable Diffusion 4x Upscaler [30] as the final super-resolution stage.

- **VQ.de-tokenizer**. The final component operates in discrete token space, i.e., $\mathbb{S}^d := \mathbb{Q}^p$, where \mathbb{Q} is a learned codebook and p denotes the number of spatial tokens (i.e., divided image patches) in the quantized representation. There are three common contexts for \mathbf{z} : (1) **Next-token auto-regression**, where tokens are predicted sequentially and the VQ decoder transforms them back into image pixels, as in Emu 3 [38], JanusPro [8], and LlamaGen [35]. (2) **Next-scale autoregression**, where the generator starts from coarse-scale tokens (e.g., a 1×1 token map) and progressively predicts higher-resolution token maps con-

Algorithm 1 Negative sample construction from *VAE_1.1*

Input: A real image set $\mathcal{D} = \{\mathbf{x}\}$
Output: The constructed image set $\{\hat{\mathbf{x}}\}$

```

1: vae=AutoencoderKL.from_pretrained
   ("sd-2-1", subfolder="vae")
2: for each  $\mathbf{x}$  in  $\mathcal{D}$  do
3:    $\mathbf{z}$  = vae.encode( $\mathbf{x}$ )
4:    $\hat{\mathbf{x}}$  = vae.decode( $\mathbf{z}$ )
5: end for
6: return  $\{\hat{\mathbf{x}}\}$ 

```

Algorithm 2 Negative sample construction from *VQ_2.2*

Input: A real image set $\mathcal{D} = \{\mathbf{x}\}$
Output: The constructed image set $\{\hat{\mathbf{x}}\}$

```

1: vq=AutoModelForCausalLM.from_
   _pretrained("janus").vq_model
2: for each  $\mathbf{x}$  in  $\mathcal{D}$  do
3:    $\mathbf{z}$  = vq.quantize(vq.encode( $\mathbf{x}$ ))
4:    $\hat{\mathbf{x}}$  = vq.decode( $\mathbf{z}$ )
5: end for
6: return  $\{\hat{\mathbf{x}}\}$ 

```

Algorithm 3 Negative sample construction from *Super-resolution_3.3*

Input: A real image set $\mathcal{D} = \{\mathbf{x}\}$
Output: The constructed image set $\{\hat{\mathbf{x}}\}$

```

1: denoiser=PixelFlow("model.pt")
2: for each  $\mathbf{x}$  in  $\mathcal{D}$  do
3:    $\mathbf{z} = \hat{\mathbf{x}}_T = \alpha\mathbf{x} + \beta\epsilon$ ,  $\epsilon \sim N(\mathbf{0}, \mathbf{I})$ 
4:   for  $t = T - 1$  to 0 do
5:      $\tilde{\epsilon}$ =denoiser( $\hat{\mathbf{x}}_{t+1}$ )
6:      $\hat{\mathbf{x}}_t = \text{step}(\hat{\mathbf{x}}_{t+1}, \tilde{\epsilon})$ 
7:   end for
8: end for
9: return  $\{\hat{\mathbf{x}}_0\}$ 

```

ditioned on all previous ones, as in VAR [36] and Infintiy [12]. (3) **Latent diffusion hybrid**, which combines global latent diffusion for coarse image structure with autoregressive token prediction for sequentially refining discrete latent components, e.g., Kandinsky [2].

- **Diffusion.denoiser.** In this category, the final step is denoising, applied over three typical input spaces. (1) **Continuous token:** $\mathbb{S}^d := \mathbb{R}^p$. The image is divided into p patches, with tokens represented as continuous embeddings rather than discrete codes. MAR [20] exemplifies this approach, as illustrated in Fig.1(d). (2) **Low-resolution image:** $\mathbb{S}^d := \mathbb{R}^{h_l \times w_l \times 3}$, where $h_l < h, w_l < w$. In this setting, the generator builds images progressively from low to high resolution through multiple upscaling stages, e.g., $64 \times 64 \rightarrow 256 \times 256 \rightarrow 1024 \times 1024$. The final step adds noise to the previous resolution’s image, resizes it to the target size, and applies diffusion denoising. This process is similar to *VAE.decoder-latent super-resolution* but operates directly in pixel space (see Fig.1(e)). Two training strategies are common: **cascade super-resolution**, where each adjacent low-to-high resolution stage is trained separately (e.g., DALL·E 3 [26] and GLIDE [24]), and **end-to-end super-resolution**, where all stages are trained jointly (e.g., PixelFlow [7]). (3) **Same-size pixels:** $\mathbb{S}^d := \mathbb{R}^{h \times w \times 3}$. The input \mathbf{z} has the same spatial resolution as the target image. It can either represent a low-quality image to be refined by the diffusion denoiser, as in ReflectionFlow [47], or an initial Gaussian noise sample used in conventional diffusion models such as DDPM [13] and DDIM [33] (Fig.1(f)).
- **One-stop.generator.** In this setting, $\mathbb{S}^d := \mathcal{N}(\mathbf{0}, \mathbf{I}_d)$. The generator directly maps a sampled noise vector to the final image, as shown in Fig.1(g). This category includes GAN-based approaches such as GigaGAN [14], which produce high-resolution images through large-scale adversarial training, and pixel-wise auto-regressive models like JetFormer [37], which generate images sequentially

in an end-to-end fashion.

The categorization of these representative generators in our proposed taxonomy is based on their official source code or released documentation, with detailed references provided in the Appendix.

3.2. Fake sample construction — $\varphi \circ \mathcal{E}$

3.2.1. Construction from the three representative components

To investigate the generalization of final component φ in generated trace detection (Eq. 1), we identify three representative final components from open-source generators in our taxonomy as shown in Fig.1: Stable Diffusion 2.1 (VAE.decoder-1.1:Latent diffusion), JanusPro (VQ.de-tokenizer-2.2:Next-token auto-regression), and PixelFlow (Diffusion.denoiser-3.3:End-to-end super-resolution). For brevity, we refer to these specific components as *VAE_1.1*, *VQ_2.2*, and *Super-resolution_3.3* respectively in the following sections. As discussed in Property 1 (Sec. 3), the encoder \mathcal{E}^* , which is pretrained jointly with φ^* , is used to approximate the latent input \mathbf{z} .

Algorithm 1 presents the pseudocode for constructing $\varphi^*(\mathcal{E}^*(\mathbf{x}))$ using the *VAE_1.1*. The implementation requires only a few lines of code and is significantly more efficient than executing the full generative pipeline. For *VQ_2.2*, the de-tokenizer acts as φ^* and the image tokenizer as \mathcal{E}^* to approximate image tokens \mathbf{z} , as outlined in Algorithm 2. In *Super-resolution_3.3*, the input \mathbf{z} is a noisy version of the real image, $\alpha\mathbf{x} + \beta\epsilon_t$, where $\epsilon \sim \mathcal{N}(0, \mathbf{I})$. The noise level can be adjusted by selecting the starting timestep t for denoising (Algorithm 3).

3.2.2. Sparse Sampling from Combined Constructions

The three final components differ substantially in both functionality and implementation. Consequently, the constructed samples $\varphi^*(\mathcal{E}^*(\mathbf{x}))$ from each reflect distinct generative traces. We further investigate whether combining

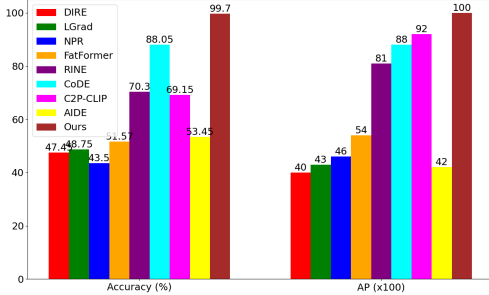


Figure 3. Performance comparison of our model trained on the final component of SD2

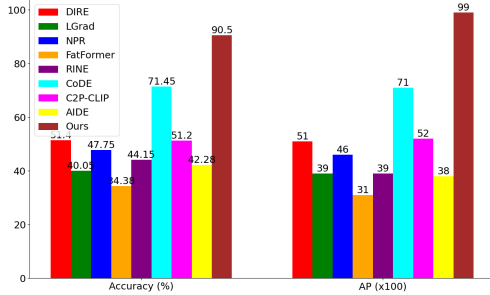


Figure 4. Performance comparison of our model trained on the final component of HiDream

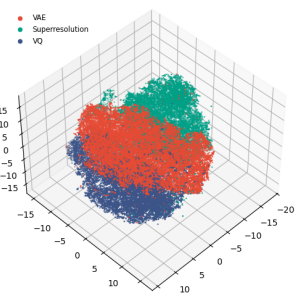


Figure 5. Feature visualization of the three final components.

Algorithm 4 Negative sample selection

Input: Constructed image sets $\mathcal{D}_1 \cup \mathcal{D}_2 \cup \mathcal{D}_3 = \{\hat{\mathbf{x}}\}_{VAE} \cup \{\hat{\mathbf{x}}\}_{VQ} \cup \{\hat{\mathbf{x}}\}_{sup}$, the number of samples to be selected k
Output: The sparse constructed image set $\{\hat{\mathbf{x}}\}$

```

1: dinov3 = torch.hub.load("dinov3_with16plus")
2: for  $i = 1$  to  $3$  do
3:   features.append(dinov3( $\hat{\mathbf{x}}$ )) for all  $\hat{\mathbf{x}} \in \mathcal{D}_i$ 
4:   dist = sklearn.metrics.euclidean_distances(features)
5:    $\mathcal{M}_i = \text{sklearn.kmedoids.fasterpam}(dist, k)$ 
      //a set of  $k$  samples of  $\hat{\mathbf{x}}$ 
6: end for
7: return  $\mathcal{M}_1 \cup \mathcal{M}_2 \cup \mathcal{M}_3$ 
```

a small number of representative fake samples from each component can better capture the overall trace space and improve generalization. Algorithm 4 outlines the procedure, applying K-Medoids clustering selects k representative samples from the constructed outputs of each component, as described in Section 3.2.1. The selection is performed in a reduced-dimensional feature space. Specifically, the generated samples are first encoded using a pre-trained DINoV3 backbone, from which 2,048-dimensional feature vectors are extracted from the final layer. K-Medoids selects k samples such that most other samples are close to one of them in Euclidean distance. The selected subsets from all three components are combined to form the final training set of $\varphi^*(\mathcal{E}^*(\mathbf{x}))$ for detector training.

3.3. Detection model — θ

Based on Property 2 discussed in Section 3, instead of loading \mathbf{x} and computing $\varphi^*(\mathcal{E}^*(\mathbf{x}))$ at each training step, we directly input the real image set (positive samples) $\{\mathbf{x}\}$ and the constructed image set $\{\hat{\mathbf{x}}\}$ generated by Algorithms 1–4, with standard shuffling applied to both sets during SGD training. Since the detector θ aims to distinguish subtle differences between real and reconstructed images, and object detection tasks inherently emphasize multi-scale spatial features, we adopt DINoV3—a foundation model pre-

trained for object detection—as the backbone to better capture fine-grained artifacts. A single fully connected layer is appended to the backbone, and all layers are fine-tuned during training. As our focus is on analyzing the effect of the final generative component, we employ a pretrained visual backbone with minimal modifications rather than designing a complex detector.

4. Experiments

4.1. Model implementation & baselines

The real image set used for constructing the training dataset is MS-COCO 2014 [21], which contains 118,000 images depicting diverse indoor and outdoor scenes with resolutions ranging from 384 to 880 pixels in width (height). The constructed training and corresponding test sets are described separately for each of the following experimental questions, with all pretrained models referenced in the Appendix.

For our AI-generated image detector, we use the pretrained backbone of DINoV3¹ with an additional fully connected layer for binary classification. All layers are fine-tuned using standard cross-entropy loss with a learning rate of 5e-7. This implementation serves as the detector for all subsequent analyses.

We compare our method against eight baseline approaches: AIDE [28] (ICLR 2025), C2P-CLIP [44] (AAAI 2025), CoDE [19] (ECCV 2024), RINE [23] (ECCV 2024), FatFormer [22] (CVPR 2024), NPR [18] (CVPR 2024), LGrad [10] (CVPR 2023), and DIRE [16] (ICCV 2023). As none of these methods report results on our testing sets, we re-evaluate all of them using their publicly released pretrained models and default hyperparameters. The source code links, parameters, and models used are detailed in the Appendix. Performance is assessed using two standard metrics: classification accuracy and average precision (AP).

Table 2.Detection results across different category of generators.

	vae.decoder based										diffusion.denoiser.super-resolution based				vq.decoder based					
	SD1.3		SD1.4		SD XL		Flux		SD 3.5		DALL-E 2		DALL-E 3		Glide		Emu3		LlamaGen	
	Acc	AP	Acc	AP	Acc	AP	Acc	AP	Acc	AP	Acc	AP	Acc	AP	Acc	AP	Acc	AP	Acc	AP
DIRE (ICCV2023)	48.75	0.43	48.65	0.43	50.00	0.59	61.66	0.73	55.65	0.59	56.45	0.67	50.35	0.54	49.50	0.49	53.65	0.57	54.05	0.59
LGrad (CVPR2023)	54.45	0.46	55.85	0.48	52.60	0.48	81.91	0.92	77.29	0.87	55.65	0.56	47.65	0.40	47.45	0.52	54.80	0.48	60.70	0.63
NPR (CVPR2024)	50.70	0.51	50.60	0.52	52.45	0.56	90.00	0.92	88.04	0.90	49.25	0.50	50.35	0.51	48.80	0.51	51.70	0.53	52.25	0.55
FatFormer (CVPR2024)	52.97	0.54	53.72	0.54	66.67	0.75	55.32	0.90	75.86	0.95	54.12	0.56	35.88	0.34	67.77	0.76	63.72	0.66	77.21	0.87
RINE (ECCV2024)	87.60	0.96	87.15	0.96	74.60	0.86	51.70	0.87	96.49	0.99	85.90	0.94	42.35	0.31	63.95	0.72	62.10	0.70	90.65	0.98
CoDE (ECCV2024)	97.75	0.97	97.30	0.97	75.20	0.75	71.09	0.72	76.35	0.75	54.60	0.54	73.15	0.73	80.75	0.80	77.45	0.77	90.50	0.90
C2P-CLIP (AAAI2025)	75.15	0.93	76.70	0.93	77.70	0.95	53.96	0.97	80.88	0.99	55.60	0.77	63.20	0.90	86.65	0.97	68.70	0.91	83.80	0.98
AIDE (ICLR2025)	57.60	0.60	56.70	0.60	62.70	0.64	98.50	0.99	96.45	0.99	59.75	0.43	14.15	0.31	59.75	0.77	62.50	0.57	63.25	0.85
Ours_vae_1.1	99.70	1.0	99.70	1.0	99.70	1.0	99.17	.9998	99.96	1.0	99.60	1.0	99.70	.9999	98.85	.9992	99.70	.9999	99.70	.9999
Ours_vq_2.2	99.85	1.0	99.85	1.0	99.85	1.0	99.19	.9997	99.82	.9999	99.80	1.0	99.85	.9999	98.75	.9984	99.85	.9999	99.85	1.0
Ours_super_res_3.3	99.90	1.0	99.80	1.0	99.90	1.0	99.89	1.0	99.86	1.0	99.35	.9991	99.85	1.0	98.60	.9985	99.90	1.0	99.90	1.0
Ours_sparse	99.15	.9990	99.15	.9990	99.15	.9988	98.95	.9828	98.98	.9958	99.80	.9987	99.15	.9991	98.05	.9947	99.15	.9990	99.15	.9982

4.2. Results & discussions

In experiments, we aim to address the following questions:

Q1: Are traces from the final component alone sufficient to detect images generated by its full pipeline?

To verify this, we train two detectors on samples from the VAE decoders of SD2 and HiDream-I1 and evaluate them on images produced by their respective full generation pipelines.

Dataset: (1) SD2. The training samples comprise real MS-COCO images and corresponding fake images constructed via Algorithm 1 using Stable Diffusion 2.1. The test set includes 1,000 real images and 1,000 SD2-generated images from Synthbuster². **(2) HiDream-I1.** The fake training samples are constructed in same procedure but using the HiDream-I1 model, and the test set is generated from the same 1,000 prompts as Synthbuster.

Fig.s 3 and 4 show that both detectors perform strongly. For SD2, baselines vary widely. CoDE and C2P-CLIP achieve relatively high results because their training sets include SD2-generated images, making this an in-distribution evaluation. In contrast, HiDream-I1 evaluation is fully zero-shot. For the AP metric, our detector achieves nearly perfect scores, with logits for real samples approaching 1 and those for fake samples approaching 0. These results demonstrate that training with the generator’s final component generalizes effectively to the generator’s full outputs.

Q2: Are traces from the final component sufficient to detect images from full pipelines across categories?

We train detectors on the three representative final components (Section 3.2.1) and an additional detector on the sparse image set (Section 3.2.2), then evaluate them on images from different categories in our taxonomy.

Dataset: Training sets. For the *VAE_1.1*, *VQ_2.2*, and *Super-Resolution_3.3* components, real images are from MS-COCO, and fake samples are constructed following Algorithms 1–3. These three types of final components ex-

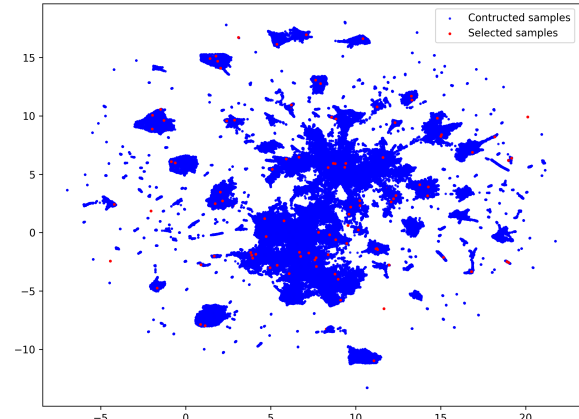


Figure 6. Sparse sample selection.

hibit distinct generation traces, visualized in Fig. 5. Features are extracted from the third layer of the pretrained DINOv3 backbone and project into three dimensions. The resulting distributions appear mixed yet remain visually separable. The sparse training set is selected using Algorithm 4, with $k = 100$. As shown in Fig. 6, the selected data points (highlighted in red) span the entire space. **Testing set.** The testing set consists of image subsets from the Synthbuster benchmark, generated by SD1.3, SD1.4, SD XL, DALL-E 2, DALL-E 3, and Glide. We categorize these subsets according to our taxonomy, as summarized in Table 6. For the VQ decoder category, we generate fake images from two autoregressive generators, Emu3 and LlamaGen, using the 1,000 Synthbuster prompts. For emerging generators Flux-dev and SD3.5, we produce 10,000 fake images each. As paired real images are unavailable, we use 9,600 real images from the PASCAL VOC training split [11] for evaluation.

Table 6 reports detection results across generator categories. Each row in the last group corresponds to a detector trained on one of the four training sets—*VAE_1.1*, *VQ_2.2*, *Super-resolution_3.3*, or the sparse set. Our approach performs strongly within the same category and generalizes well across categories. For example, on DALL-E 2—where

¹<https://huggingface.co/facebook/dinov3-vith16plus-pretrain-lvd1689m>

²<https://zenodo.org/records/10066460>

Table 3. Detection results on unknown generators.

	Unknown		Mixture		Wild							
	Firefly		Midjourney		FakeBench		Reddit		Facebook		Twitter	
	Acc	AP										
DIRE	50.8	0.55	53.9	0.61	44.38	0.42	57.19	0.62	56.56	0.66	47.74	0.79
LGrad	47.25	0.42	57.7	0.53	44.01	0.69	57.80	0.65	66.88	0.77	40.86	0.61
NPR	47.30	0.47	52.35	0.55	52.37	0.58	63.80	0.67	74.06	0.84	48.46	0.68
FatFormer	60.12	0.62	44.43	0.42	71.2	0.81	69.47	0.81	54.83	0.75	42.79	0.77
RINE	92.10	0.99	55.45	0.59	74.77	0.97	71.20	0.81	51.56	0.55	55.93	0.62
CoDE	60.65	0.60	76.90	0.77	74.75	0.74	65.8	0.61	72.19	0.67	68.41	0.78
C2P-CLIP	59.45	0.82	52.85	0.69	74.77	0.91	68.40	0.79	54.37	0.71	47.27	0.75
AIDE	14.40	0.32	53.45	0.40	74.78	0.87	70.87	0.83	50.00	0.56	52.78	0.59
Ours_vae_1.1	99.70	1.0	99.70	.9999	98.83	.9997	96.87	.9968	97.81	.9899	98.34	.9993
Ours_vq_2.2	99.70	.9999	99.45	.9996	98.10	.9982	95.40	.9980	95.31	.9928	98.34	.9986
Ours_sup-res	98.50	.9996	99.70	1.0	94.38	.9978	98.67	.9964	97.19	.9946	97.39	.9998
Ours_sparse	98.00	.9973	99.10	.9990	97.90	.9991	97.60	.9951	98.44	.9944	99.31	1.0

most baselines are near random (e.g., NPR: 49.20%, LGrad: 55.65%, FatFormer: 54.12%)—only CLIP-based models like RINE (85.90%) and AIDE (59.75%) show moderate gains, benefiting from DALL-E 2’s CLIP-based design. Despite not relying on CLIP features, our method achieves substantially higher accuracy, highlighting robust generalization to unseen generator architectures.

Notably, the detector trained on the sparse set, using only 100 fake samples from each of the three components (300 fake and 300 real images in total), achieves performance comparable to our three models trained on individual components with the full MS-COCO dataset. This small training set provides further evidence of the generalization capability of our approach and offers a practical advantage, as generating large-scale training images is costly.

Q3: Are traces from the final component sufficient to detect images from wild or unknown generators?

The detectors trained for Q2 are directly evaluated on testing sets for this question.

Dataset: Testing set. **(1) Unknown generators**—Firefly and Midjourney test sets from Synthbuster. Both are commercial generators lacking open-source code or public documentation of their architectures or components. **(2) Mixed generators—FakeBench**³ benchmark contains 3,000 real images and 3,000 fake images generated by multiple models. **(3) In-the-wild generation—WildRF**⁴ comprises three subsets: Reddit, Facebook, and Twitter, each containing real and synthetic images sourced from social media platforms with unknown origins.

Table 3 reports the results. Baseline methods exhibit highly inconsistent results across benchmarks. For instance, RINE performs well on Firefly (92.10% accuracy, 0.99 AP) but drops sharply on Midjourney (55.45%) and Facebook (51.56%), while AIDE misclassifies most samples—achieving only 14.40% accuracy. This instability highlights the challenge of real-world generalization, particularly in true zero-shot scenarios where no prior infor-

³<https://github.com/Yixuan423/FakeBench>

⁴<https://vision.huji.ac.il/ladeda/>

Table 4. Results on finetuned generators.

Unknown		Mixture		Wild						Satellite image generation						
Firefly	Midjourney	Firefly	Midjourney	FakeBench	Reddit	Facebook	Twitter	amuse_park	car_dealership	electric_station	stadium	amuse_park	car_dealership	electric_station	stadium	
Acc	AP	Acc	AP	Acc	AP	Acc	AP									
50.8	0.55	53.9	0.61	44.38	0.42	57.19	0.62	56.56	0.66	47.74	0.79	50.49	0.86	50.19	0.84	
47.25	0.42	57.7	0.53	44.01	0.69	57.80	0.65	66.88	0.77	40.86	0.61	48.85	0.36	50.00	0.42	
47.30	0.47	52.35	0.55	52.37	0.58	63.80	0.67	74.06	0.84	48.46	0.68	46.89	0.43	65.52	0.84	
60.12	0.62	44.43	0.42	71.2	0.81	69.47	0.81	54.83	0.75	42.79	0.77	51.68	0.70	50.88	0.83	
92.10	0.99	55.45	0.59	74.77	0.97	71.20	0.81	51.56	0.55	55.93	0.62	69.07	0.83	51.97	0.50	
60.65	0.60	76.90	0.77	74.75	0.74	65.8	0.61	72.19	0.67	68.41	0.78	86.66	0.82	88.40	0.84	
59.45	0.82	52.85	0.69	74.77	0.91	68.40	0.79	54.37	0.71	47.27	0.75	58.00	0.76	76.60	0.96	
14.40	0.32	53.45	0.40	74.78	0.87	70.87	0.83	50.00	0.56	52.78	0.59	52.90	0.58	61.71	0.85	
Ours_vae_1.1	99.70	1.0	99.70	.9999	98.83	.9997	96.87	.9968	97.81	.9899	98.34	.9993	99.33	1.0	96.43	.9996
Ours_vq_2.2	99.70	.9999	99.45	.9996	98.10	.9982	95.40	.9980	95.31	.9928	98.34	.9986	96.77	1.0	87.52	.9998
Ours_sup-res	98.50	.9996	99.70	1.0	94.38	.9978	98.67	.9964	97.19	.9946	97.39	.9998	99.67	.9997	97.94	.9962
Ours_sparse	98.00	.9973	99.10	.9990	97.90	.9991	97.60	.9951	98.44	.9944	99.31	1.0	99.61	.9999	98.91	.9994

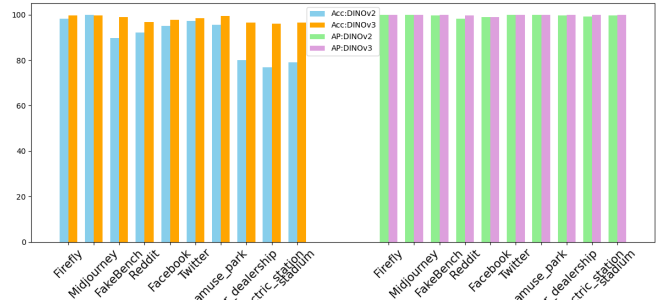


Figure 7. Performances of our detectors with different backbones

mation about the generators is available. In contrast, our detector consistently surpasses all baselines and maintains robust, stable performance across all subsets, demonstrating that leveraging traces from the final component yields strong generalization to diverse architectures and challenging real-world conditions.

Q4: Does detection performance on a full generator remain valid after fine-tuning the generator?

The detectors trained for Q2 are directly evaluated on testing sets for this question.

Dataset: Testing set — **SatelliteDiffusion**^[15] dataset is generated using a domain-specific model fine-tuned from SD2, conditioned on satellite metadata. Real images are sourced from high-resolution satellite imagery, while synthetic counterparts are produced using textual descriptions of the real samples. Four subsets: *amusement park*, *car dealership*, *electric substation*, and *stadium* are tested, each including around 2,000 real and 2,000 generated images.

Table 4 presents the comparison. Our models attain results closely matching those reported for the original SD2 evaluations (Fig. 3, Table 6), demonstrating that detection remains effective for generators fine-tuned on domain-specific images and conditions.

Q5: How does the classification backbone affect detection performance? To evaluate the impact of the backbone on our detector, we train a model using a pretrained

DINOv2 backbone on the VAE training set used in the previous experiments. We compare the performance of DINOv2 and DINOv3 on the testing sets from Q3 and Q4 (Fig. 7). The results show that the newer backbone provides a significant improvement in accuracy. For AP, since the margin between the logits of positive and negative images is sufficiently large with DINOv2, using the newer backbone has little effect.

5. Conclusion

This study demonstrates that leveraging the final components of modern image generators offers a powerful means to enhance deepfake detection generalization. By contaminating real images through these components and training on minimal representative samples, the proposed detector achieves superior performance across diverse unseen generators, highlighting the value of insights for robust detection.

References

- [1] Lydia Abady, Jun Wang, Benedetta Tondi, and Mauro Barni. A siamese-based verification system for open-set architecture attribution of synthetic images. *Pattern Recognition Letters*, 180:75–81, 2024. 3
- [2] Vladimir Arkhipkin, Andrei Filatov, Viacheslav Vasilev, Anastasia Maltseva, Said Azizov, Igor Pavlov, Julia Agafonova, Andrey Kuznetsov, and Denis Dimitrov. Kandinsky 3.0 technical report. *arXiv preprint arXiv:2312.03511*, 2023. 5
- [3] Léon Bottou. Large-scale machine learning with stochastic gradient descent. In *Proceedings of the 19th International Conference on Computational Statistics (COMPSTAT'2010)*, pages 177–187, Paris, France, 2010. Springer. 4
- [4] Qi Cai, Jingwen Chen, Yang Chen, Yehao Li, Fuchen Long, Yingwei Pan, Zhaofan Qiu, Yiheng Zhang, Fengbin Gao, Peihan Xu, et al. Hidream-i1: A high-efficient image generative foundation model with sparse diffusion transformer. *arXiv preprint arXiv:2505.22705*, 2025. 4
- [5] Li-Wen Chang, Wenlei Bao, Qi Hou, Chengquan Jiang, Ningxin Zheng, Yinmin Zhong, Xuanrun Zhang, Zuquan Song, Chengji Yao, Ziheng Jiang, et al. Flux: fast software-based communication overlap on gpus through kernel fusion. *arXiv preprint arXiv:2406.06858*, 2024. 4
- [6] Nora Chen and Oscar Gupta. Lasted: Label-aware synthetic/real text embedding detection. In *CVPR*, 2024. 3
- [7] Shoufa Chen, Chongjian Ge, Shilong Zhang, Peize Sun, and Ping Luo. Pixelflow: Pixel-space generative models with flow. *arXiv preprint arXiv:2504.07963*, 2025. 5
- [8] Xiaokang Chen, Zhiyu Wu, Xingchao Liu, Zizheng Pan, Wen Liu, Zhenda Xie, Xingkai Yu, and Chong Ruan. Janus-pro: Unified multimodal understanding and generation with data and model scaling. *arXiv preprint arXiv:2501.17811*, 2025. 4
- [9] DeepFloydTeam. Deepfloyd if. <https://github.com/deep-floyd/IF>, 2024. 4
- [10] Jane Doe and John Smith. Lgrad: Gradient-based fingerprint detection for deepfakes. In *CVPR*, 2023. 1, 3, 6
- [11] Mark Everingham, Luc Van Gool, Christopher K. I. Williams, John Winn, and Andrew Zisserman. The PASCAL visual object classes (voc) challenge 2007, 2007. <http://host.robots.ox.ac.uk/pascal/VOC/voc2007/>. 7
- [12] Jian Han, Jinlai Liu, Yi Jiang, Bin Yan, Yuqi Zhang, Zehuan Yuan, Bingyue Peng, and Xiaobing Liu. Infinity: Scaling bit-wise autoregressive modeling for high-resolution image synthesis, 2024. 5
- [13] Jonathan Ho, Ajay Jain, and Pieter Abbeel. Denoising diffusion probabilistic models. *Advances in neural information processing systems*, 33:6840–6851, 2020. 1, 5
- [14] Minguk Kang, Jun-Yan Zhu, Richard Zhang, Jaesik Park, Eli Shechtman, Sylvain Paris, and Taesung Park. Scaling up gans for text-to-image synthesis. In *Proceedings of the IEEE Conference on Computer Vision and Pattern Recognition (CVPR)*, 2023. 5
- [15] Samar Khanna, Patrick Liu, Linqi Zhou, Chenlin Meng, Robin Rombach, Marshall Burke, David B Lobell, and Stefano Ermon. Diffusionsat: A generative foundation model for satellite imagery. In *The Twelfth International Conference on Learning Representations*, 2023. 8
- [16] Claire Kim and David Johnson. Dire: Decoder-invertible fingerprint recovery. In *ICCV*, 2023. 1, 3, 6
- [17] Mike Laszkiewicz, Jonas Ricker, Johannes Lederer, and Asja Fischer. Single-model attribution of generative models through final-layer inversion. *arXiv preprint arXiv:2306.06210*, 2023. 3
- [18] Alice Lee and Bob Wang. Npr: Pixel neighborhood difference fingerprints for fake image detection. In *CVPR*, 2024. 3, 6
- [19] Ryan Li and Sophie Davis. Code: Contrastive detection engine for multi-scale fake image features. In *ECCV*, 2024. 1, 3, 6
- [20] Tianhong Li, Yonglong Tian, He Li, Mingyang Deng, and Kaiming He. Autoregressive image generation without vector quantization. *Advances in Neural Information Processing Systems*, 37:56424–56445, 2024. 4, 5
- [21] Tsung-Yi Lin, Michael Maire, Serge Belongie, James Hays, Pietro Perona, Deva Ramanan, Piotr Dollár, and C. Lawrence Zitnick. Microsoft coco: Common objects in context. *European conference on computer vision*, pages 740–755, 2014. 6
- [22] Huan Liu, Zichang Tan, Chuangchuang Tan, Yunchao Wei, Jingdong Wang, and Yao Zhao. Forgery-aware adaptive transformer for generalizable synthetic image detection. In *Proceedings of the IEEE/CVF Conference on Computer Vision and Pattern Recognition*, pages 10770–10780, 2024. 6
- [23] George Nguyen and Helen Martinez. Rine: Clip-enhanced deepfake detection via representation integration. *arXiv preprint arXiv:2403.54321*, 2024. 3, 6
- [24] Alex Nichol and Prafulla Dhariwal. Glide: Towards photo-realistic image generation and editing with text-guided diffusion models. *arXiv preprint arXiv:2112.10741*, 2021. 5
- [25] Ian Olson and Karen Cho. Defake: Text-guided deepfake detection. In *SIGSAC*, 2023. 3

[26] OpenAI. Introducing dall-e 3. <https://openai.com/all-e-3>, 2023. 5

[27] OpenAI. Gpt-4o: Openai’s new multimodal model. <https://openai.com/index/gpt-4o>, 2024. Accessed: 2025-07-26. 1

[28] Priya Patel and Quinn Lopez. Aide: Adversarial-inspired detection with frequency domain features. In *ICLR*, 2025. 1, 3, 6

[29] Herbert Robbins and Sutton Monro. A stochastic approximation method. *Annals of Mathematical Statistics*, 22(3): 400–407, 1951. 4

[30] Robin Rombach, Andreas Blattmann, Dominik Lorenz, Patrick Esser, and Björn Ommer. High-resolution image synthesis with latent diffusion models. In *Proceedings of the IEEE/CVF Conference on Computer Vision and Pattern Recognition (CVPR)*, pages 10684–10695, 2022. 4

[31] Sowdagar Mohammad Shahid, Sudev Kumar Padhi, Umesh Kashyap, and Sk Subidh Ali. Generalized deepfake attribution. *arXiv preprint arXiv:2406.18278*, 2024. 3

[32] Oriane Siméoni, Huy V Vo, Maximilian Seitzer, Federico Baldassarre, Maxime Oquab, Cijo Jose, Vasil Khalidov, Marc Szafraniec, Seungeun Yi, Michaël Ramamonjisoa, et al. Dinov3. *arXiv preprint arXiv:2508.10104*, 2025. 2

[33] Jiaming Song, Chenlin Meng, and Stefano Ermon. Denoising diffusion implicit models. In *International Conference on Learning Representations*, 2020. 5

[34] StabilityAI. Introducing stable diffusion 3.5. <https://stability.ai/news/introducing-stable-diffusion-3-5>, 2024. 4

[35] Peize Sun, Yi Jiang, Shoufa Chen, Shilong Zhang, Bingyue Peng, Ping Luo, and Zehuan Yuan. Autoregressive model beats diffusion: Llama for scalable image generation. *arXiv preprint arXiv:2406.06525*, 2024. 4

[36] Keyu Tian, Yi Jiang, Zehuan Yuan, Bingyue Peng, and Liwei Wang. Visual autoregressive modeling: Scalable image generation via next-scale prediction, 2024. 5

[37] Michael Tschannen, André Susano Pinto, and Alexander Kolesnikov. Jetformer: An autoregressive generative model of raw images and text. *arXiv preprint arXiv:2411.19722*, 2024. 5

[38] Xinlong Wang, Xiaosong Zhang, Zhengxiong Luo, Quan Sun, Yufeng Cui, Jinsheng Wang, Fan Zhang, Yueze Wang, Zhen Li, Qiying Yu, et al. Emu3: Next-token prediction is all you need. *arXiv preprint arXiv:2409.18869*, 2024. 4

[39] Zhenting Wang, Vikash Sehwag, Chen Chen, Lingjuan Lyu, Dimitris N Metaxas, and Shiqing Ma. How to trace latent generative model generated images without artificial watermark? *arXiv preprint arXiv:2405.13360*, 2024. 3

[40] Yuxiang Wei, Yiheng Zheng, Yabo Zhang, Ming Liu, Zhi-long Ji, Lei Zhang, and Wangmeng Zuo. Personalized image generation with deep generative models: A decade survey. *arXiv preprint arXiv:2502.13081*, 2025. 2

[41] Alexander Wißmann, Steffen Zeiler, Robert M Nickel, and Dorothea Kolossa. Whodunit: Detection and attribution of synthetic images by leveraging model-specific fingerprints. In *Proceedings of the 3rd ACM International Workshop on Multimedia AI against Disinformation*, pages 65–72, 2024. 3

[42] Katherine Xu, Lingzhi Zhang, and Jianbo Shi. Detecting origin attribution for text-to-image diffusion models in rgb and beyond. In *Neurips Safe Generative AI Workshop 2024*, 2024. 3

[43] Tianyun Yang, Ziyao Huang, Juan Cao, Lei Li, and Xirong Li. Deepfake network architecture attribution. In *Proceedings of the AAAI Conference on Artificial Intelligence*, pages 4662–4670, 2022. 3

[44] Leo Zhang and Maya Kumar. C2p-clip: Contrastive caption prompting for fake image detection. In *AAAI*, 2025. 1, 3, 6

[45] Wendi Zheng, Jiayan Teng, Zhuoyi Yang, Weihan Wang, Jidong Chen, Xiaotao Gu, Yuxiao Dong, Ming Ding, and Jie Tang. Cogview3: Finer and faster text-to-image generation via relay diffusion. In *European Conference on Computer Vision*, pages 1–22. Springer, 2024. 4

[46] Emily Zhou and Frank Patel. Univfd: Universal deepfake detection with clip image features. *arXiv preprint arXiv:2402.12345*, 2024. 3

[47] Le Zhuo, Liangbing Zhao, Sayak Paul, Yue Liao, Renrui Zhang, Yi Xin, Peng Gao, Mohamed Elhoseiny, and Hongsheng Li. From reflection to perfection: Scaling inference-time optimization for text-to-image diffusion models via reflection tuning. *arXiv preprint arXiv:2504.16080*, 2025. 5

Exploiting the Final Component of Generator Architectures for AI-Generated Image Detection

Supplementary Material

6. Discussion on Property 2

For convenience, the paired gradient $\hat{\nabla}_\theta^{\text{paired}}$ can be rewritten as:

$$\hat{\nabla}_\theta^{\text{paired}} = -\frac{1}{|\mathcal{B}_t|} \sum_{i=1}^{|\mathcal{B}_t|} \left[\nabla_\theta \log \theta(\mathbf{x}_i) + \nabla_\theta \log(1 - \theta(\varphi(\mathcal{E}(\mathbf{x}_i)))) \right].$$

Define

$$g_i = \nabla_\theta \log \theta(\mathbf{x}_i), \quad g'_i = \nabla_\theta \log(1 - \theta(\varphi(\mathcal{E}(\mathbf{x}_i)))),$$

and let

$$G = \{g_i\}_{i=1}^{|\mathcal{B}_t|}, \quad G' = \{g'_i\}_{i=1}^{|\mathcal{B}_t|}.$$

Under this notation, $\hat{\nabla}_\theta^{\text{paired}}$ becomes

$$\hat{\nabla}_\theta^{\text{paired}} = -\frac{1}{|\mathcal{B}_t|} \sum_{i=1}^{|\mathcal{B}_t|} [g_i + g'_i].$$

Since the elements of \mathcal{B}_t are sampled independently, each \mathbf{x}_i is independent of all other samples in \mathcal{B}_t . Consequently, each gradient g_i is independent of all other elements in G except itself, and the same holds for g'_i within G' . Furthermore, g_i is independent of all elements of G' except for its paired counterpart g'_i , and vice versa.

Using the fact that independent random variables have zero covariance, the variance of $\hat{\nabla}_\theta^{\text{paired}}$ is:

$$\begin{aligned} \text{Var}(\hat{\nabla}_\theta^{\text{paired}}) &= \frac{1}{|\mathcal{B}_t|} \sum_{i=1}^{|\mathcal{B}_t|} \left[\text{Var}(g_i) + \text{Var}(g'_i) + 2\text{Cov}(g_i, g'_i) \right] \\ &= \frac{1}{|\mathcal{B}_t|} \left[\text{Var}(G) + \text{Var}(G') + \text{Cov}(G, G') \right], \end{aligned}$$

where

$$\text{Var}(G) = \sum_{i=1}^{|\mathcal{B}_t|} \text{Var}(g_i), \quad \text{Var}(G') = \sum_{i=1}^{|\mathcal{B}_t|} \text{Var}(g'_i),$$

$$\text{Cov}(G, G') = 2 \sum_{i=1}^{|\mathcal{B}_t|} \text{Cov}(g_i, g'_i).$$

In contrast, the variance under independent sampling is

$$\text{Var}(\hat{\nabla}_\theta^{\text{indep}}) = \frac{1}{|\mathcal{B}_t|} \text{Var}(G) + \frac{1}{|\mathcal{B}_t|} \text{Var}(G').$$

The only difference between the two variances is the covariance term $\text{Cov}(G, G')$, which aggregates the individual

covariances between g_i and g'_i . Our key observation is that \mathbf{x}_i and its transformed version $\mathbf{x}'_i = \varphi(\mathcal{E}(\mathbf{x}_i))$ are highly similar, and thus their gradients g_i and g'_i tend to be positively correlated. Therefore, $\text{Cov}(g_i, g'_i) > 0$, implying $\text{Cov}(G, G') > 0$. As a result,

$$\text{Var}(\hat{\nabla}_\theta^{\text{paired}}) > \text{Var}(\hat{\nabla}_\theta^{\text{indep}}).$$

This confirms our claim that the gradient estimator achieves lower variance when mini-batches are sampled independently from \mathcal{D} and \mathcal{D}' .

We empirically compare pairwise training with independent training. Using samples generated by *VAE_1.1*, we train detectors with identical model architectures, hyper-parameters, and training data. The only difference lies in how mini-batches are constructed: pairwise training loads matched pairs $(\mathbf{x}, \mathbf{x}')$ into the same mini-batch, whereas independent training samples \mathbf{x} and \mathbf{x}' independently and loads them separately, while ensuring that each mini-batch contains the same number of positive samples \mathbf{x} and negative samples \mathbf{x}' . Table A reports the results. We copy the baseline numbers and *Ours_VAE_1.1* results from Table 2 of the main paper, along with the additional row for pairwise training. The average accuracy of pairwise training is 97.22%, compared to 99.22% for independent training—a 2% gap. This empirical observation suggests that pairwise training does not provide an advantage over independent training, consistent with our theoretical analysis above.

7. Evidence sources for categorization

Table B summarizes the sources used to determine the final-component category of each generator. For all open-source models, we list the exact commit version, together with the file paths and line numbers that invoke the final component. DALL·E 2 provides only documentation rather than code, and DALL·E 3 has neither detailed documentation nor public source code. Among the listed generators, Flux-1-dev has two widely used official implementations: the Diffusers version operates in latent space and uses a VAE decoder as its final component, while the Black Forest Labs implementation performs generation directly in pixel space. A similar situation appears in DeepFloyd IF: its Stage III super-resolution step has two variants—one based on the Stable Diffusion ×4 latent upsampler, and another implemented in pixel space. Moreover, although MAR is grouped under the “denoiser” category, its final step is a decoder network structurally similar to a U-Net denoiser but without any noise addition or removal.

Table A. Comparison between pairwise training and independent training.

	vae.decoder based								diffusion.denoiser.super-resolution based				vq.decoder based				Emu3		LlamaGen	
	SD1.3		SD1.4		SD XL		Flux		SD 3.5		DALL-E 2		DALL-E 3		Glide		Emu3		LlamaGen	
	Acc	AP	Acc	AP	Acc	AP	Acc	AP	Acc	AP	Acc	AP	Acc	AP	Acc	AP	Acc	AP	Acc	AP
DIRE (ICCV2023)	48.75	0.43	48.65	0.43	50.00	0.59	61.66	0.73	55.65	0.59	56.45	0.67	50.35	0.54	49.50	0.49	53.65	0.57	54.05	0.59
LGGrad (CVPR2023)	54.45	0.46	55.85	0.48	52.60	0.48	81.91	0.92	77.29	0.87	55.65	0.56	47.65	0.40	47.45	0.52	54.80	0.48	60.70	0.63
NPR (CVPR2024)	50.70	0.51	50.60	0.52	52.45	0.56	90.00	0.92	88.04	0.90	49.25	0.50	50.35	0.51	48.80	0.51	51.70	0.53	52.25	0.55
FatFormer (CVPR2024)	52.97	0.54	53.72	0.54	66.67	0.75	55.32	0.90	75.86	0.95	54.12	0.56	35.88	0.34	67.77	0.76	63.72	0.66	77.21	0.87
RINE (ECCV2024)	87.60	0.96	87.15	0.96	74.60	0.86	51.70	0.87	96.49	0.99	85.90	0.94	42.35	0.31	63.95	0.72	62.10	0.70	90.65	0.98
CoDE (ECCV2024)	97.75	0.97	97.30	0.97	75.20	0.75	71.09	0.72	76.35	0.75	54.60	0.54	73.15	0.73	80.75	0.80	77.45	0.77	90.50	0.90
C2P-CLIP (AAAI2025)	75.15	0.93	76.70	0.93	77.70	0.95	53.96	0.97	80.88	0.99	55.60	0.77	63.20	0.90	86.65	0.97	68.70	0.91	83.80	0.98
AIDE (ICLR2025)	57.60	0.60	56.70	0.60	72.60	0.64	98.50	0.99	96.45	0.99	59.75	0.43	14.15	0.31	59.75	0.77	62.50	0.57	63.25	0.85
Ours_vae_1.1	99.70	1.0	99.70	1.0	99.70	1.0	99.17	.9998	99.96	1.0	99.60	1.0	99.70	.9999	98.85	.9992	99.70	.9999	99.70	.9999
Ours_vae_1.1_pairwise	98.20	.9999	98.20	.9999	98.20	.9992	98.88	.9542	99.07	.9775	98.10	.9998	98.20	.9970	98.05	.9991	98.20	.9998	98.20	.9998

8. Baseline models

As none of the baseline methods report results on our testing sets, we re-evaluate all of them using their publicly released pretrained models and default hyperparameters. All baselines compute Accuracy and AP using the same functions from `sklearn.metrics: accuracy_score` and `average_precision_score`. The only exception is CoDE, which does not include AP computation in its evaluation code; for this case, we add the same AP calculation used by the other baselines. Below, we provide the links to the testing code and pretrained weights. For each baseline, we use the default hyperparameters specified in the authors' example scripts within their repositories.

- **DIRE** (ICCV 2023): Testing code from <https://github.com/ZhendongWang6/DIRE>. We use the pretrained model `lsun_adm.pth` downloaded from the provided checkpoints.
- **LGrad** (CVPR 2023): Testing code from <https://github.com/chuangchuangtan/LGrad>, with pretrained weights `LGrad-4class-Trainon-Program-car-cat-chair-horse.pth`.
- **NPR** (CVPR 2024): Testing code from <https://github.com/chuangchuangtan/NPR-DeepfakeDetection>, with pretrained weights `model_epoch_last_3090.pth`.
- **FatFormer** (CVPR 2024): Testing code from <https://github.com/Michel-liu/FatFormer>, using `fatformer_4class_ckpt.pth`.
- **RINE** (ECCV 2024): Testing code from <https://github.com/mever-team/rine>, using `model_ldm_trainable.pth`.
- **CoDE** (ECCV 2024): Testing code from <https://github.com/aimagelab/CoDE>, with the pretrained classifier available at https://huggingface.co/aimagelab/CoDE/tree/main/sklearn/linear_tot_classifier_epoch-32.sav.
- **C2P-CLIP** (AAAI 2025): Testing code from <https://github.com/chuangchuangtan/C2P-CLIP-DeepfakeDetection>, using the released weights at https://www.now61.com/f/950efW/C2P_CLI

P_release_20240901.zip/C2P_CLIP_release_20240901.pth.

- **AIDE (ICLR 2025):** Testing code from <https://github.com/shilinyan99/AIDE>, using `program_train.pth`.

9. Datasets construction

Based on **Property 2**, we generate the constructed image sets \mathbf{x}' offline and save them before training begins. For each of the three representative final components, the corresponding constructed training set is produced using its well-trained, optimized encoder, following the guidance of **Property 1**. Below, we list the real images and the pretrained \mathcal{E}^* and φ^* used in our experiments:

- **VAE_1.1 training set:** The real images are from the full MS-COCO 2014 dataset (118k images). The pretrained VAE used to generate negative samples is the VAE from <https://huggingface.co/stabilityai/stable-diffusion-2-1>.
- **HiDream training set in Experiment Q1:** The pretrained VAE weights are from HiDream-I1-Full <https://huggingface.co/HiDream-ai/HiDream-I1-Full>.
- **VQ_2.2 training set:** The pretrained model used for converting real images is JanusPro-7B <https://huggingface.co/deepseek-ai/Janus-Pro-7B>. Due to its fixed patch size, Janus only supports a resolution of 378×378. Therefore, we filter out images smaller than this size and center-crop the remaining MS-COCO images to 378×378.
- **Super-resolution_3.3 training set:** We use PixelFlow <https://huggingface.co/ShoufaChen/PixelFlow-Text2Image/tree/main/model.pt>, whose last stage is pretrained to upscale images from 128×128 to 512×512. For real images in MS-COCO, we crop them to 512×512 whenever the resolution allows. We do not downsample and re-upsample the real images; instead, we directly use real images that match the output resolution.
- **Sparse selection set:** We run Algorithm 4 on the constructed sample sets from *VAE_1.1*, *VQ_2.2*, and *Super-resolution_3.3*.

Table B. Sources for generator categorization.

Name	Category	Source	Evidence	
Stable Diffusion 3.5	vae.decoder	https://github.com/Stability-AI/sd3.5	Commit 106db06 sd3.infer.py : Line 495	image = self.vae_decode(sampled_latent)
Flux 1-dev	vae.decoder	https://github.com/huggingface/diffusers/tree/main/src/diffusers/pipelines/flux	Commit 5e181ed pipeline_flux.py : Line 1006	image = self.vae.decode(latents, return_dict=False) [0]
	diffusion.denoiser	https://github.com/black-forest-labs/flux	Commit 57ce405 src/flux/sampling.py : Line 351	img = img + (t.prev - t.curr) * pred
HiDream-II	vae.decoder	https://github.com/HiDream-ai/HiDream-II	Commit 3519729 hi_diffusers/pipelines/hidream.image/pipeline_hidream_image.py : Line 724	image = self.vae.decode(latents, return_dict=False) [0]
Stable diffusion xl	vae.decoder	https://github.com/huggingface/diffusers/tree/main/src/diffusers/pipelines/stable_diffusion_xl&	Commit 0d1c5b0 pipeline_stable_diffusion_xl.py : Line 1292	image = self.vae.decode(latents, return_dict=False) [0]
CogView4	vae.decoder	https://github.com/huggingface/diffusers/blob/main/src/diffusers/pipelines/cogview4	Commit 0d1c5b0 pipeline_cogview4.py : Line 673	image = self.vae.decode(latents, return_dict=False, generator=generator) [0]
DeepFloyd IF	vae.decoder	https://github.com/deep-floyd/IF/	Commit af64403 deepfloyd_if/modules/stage_III_sd_x4.py : Line 80	available_models = ['stable-diffusion-x4-upscaler'] ... images = self.model(**metadata).images
	diffusion.denoiser	https://github.com/deep-floyd/IF/	Commit a4df8db pipeline_stable_diffusion_upscale.py : Line 798	image = self.vae.decode(latents / self.vae.config.scaling_factor, return_dict=False) [0]
			Commit af64403 deepfloyd_if/modules/stage_III.py:Line 26 Commit af64403 deepfloyd_if/modules/base.py : Line 194	return super().embeddings_to_image(...) sample = diffusion.p_sample_loop(...)
Kandinsky 3.0	vq.de-tokenizer	https://github.com/ai-forever/Kandinsky-3	Commit 10db67a kandinsky3/movq.py: Line 420,421	decoder_input = self.post_quant_conv(quant) decoded = self.decoder(decoder_input, quant)
Emu3	vq.de-tokenizer	https://github.com/baaivision/Emu3	Commit 1a43ee6 emu3/mlm/processing_emu3.py : Line 198, 199	doc=self.tokenizer.decode(*args, **kwargs) return self.multimodal_decode(doc)
JanusPro	vq.de-tokenizer	https://github.com/deepseek-ai/Janus	Commit 659982f janus/models/ vq-model.py: Line 506,507	quant_b = self.quantize.get_codebook_entry() dec = self.decode(quant_b)
LlamaGen	vq.de-tokenizer	https://github.com/FoundatioNViSion/LlamaGen	Commit 5a50452 autoregressive/sample/ sample_t2i.py : Line 121	samples = vq_model.decode_code(index_sample, qzshape)
Infinity	vq.de-tokenizer	https://github.com/FoundatioNViSion/Infinity	Commit 3ab8e0c infinity/models/infinity.py : Line 636	img = vae.decode(summed_codes.squeeze(-3))
VAR	vq.de-tokenizer	https://github.com/FoundatioNViSion/VAR	Commit a5cf0a1 models/var.py : Line 190	return self.vae_proxy[0].fhat_to_img(f_hat) // self.vae_proxy: Tuple[VQVAE]
MAR	decoder	https://github.com/LTH14/mar	Commit fe1de72 models/mar.py : Line: 225	x = block(x)
DALL-E 2	diffusion.denoiser	Document: Hierarchical Text-ConditionalImage Generation with CLIP Latents	Page 4	“we train two diffusion upsampler models: one to upsample images from 64x64 to 256x256 resolution, and another to further upsample those to 1024x1024 resolution”
GLIDE	diffusion.denoiser	https://github.com/openai/glide-text2im	Commit 1f791b8 glide_text2im/text2im_model.py: Line 167	return super().forward(x, timesteps, **kwargs)
PixelFlow	diffusion.denoiser	https://github.com/ShoufaChen/PixelFlow	Commit eeabc08 pixelflow/pipeline_pixelflow.py : Line 253	latents = self.scheduler.step(model_output=noise_pred, sample=latents)
Reflection-Flow	diffusion.denoiser	https://github.com/Diffusion-CoT/ReflectionFlow	train_flux /sample.py : inference-time refine by black-forest-labs/FLUX.1-dev	Flux-1-dev (pixel-space implmentation; see note above)
DDPM	diffusion.denoiser	https://github.com/hojonatha/nho/diffusion	Commit c461299 diffusion_tf/diffusion_utils_2.py : Line 211	self.p.sample(..., x=img_, ...)
DDIM	diffusion.denoiser	https://github.com/huggingface/diffusers/tree/main/src/diffusers/pipelines/ddim	Commit a4df8db pipeline_ddim.py : Line 152	image = self.scheduler.step(...)
GigaGAN	one-stop.generator	https://github.com/lucidrains/gigagan-pytorch	Commit 0806433 gigagan_pytorch/gigagan_pytorch.py: Line 2167, 2169	model = self.G_ema if self.has_ema_generator else self.G return model(*args, **kwargs)
JetFormer	one-stop.generator	https://github.com/google-research/big_vision	Commit 9c006bf big_vision/models/proj/jetformer/jetformer.py: Line 481	prelogits, decoder_out = self.decoder(x, ...)

resolution_3.3. Once the constructed (negative) samples are selected, their corresponding real images form the positive training set.

For the testing set, we use the full sets from the benchmarks Synthbuster, FakeBench, and WildRF. In Synthbuster, there are 1,000 high-resolution real images from RAISE-1K, along with 1,000 fake images generated by each of nine models: DALL-E2, DALL-E3, Adobe Firefly, MidJourney v5, SD1.3, SD1.4, SD2, SDXL, and Glide. The corresponding columns in Tables 2 and 3 correspond to these subsets. To include more recent generators, we additionally construct the following test sets used in the experiments reported in the main paper:

- **HiDream (Q1), Emu3, and LlamaGen (Q2):** Real images are the same as in Synthbuster. Fake images are generated from the same 1,000 prompts used for the original nine generators (listed in `prompts.csv` in <https://zenodo.org/records/10066460/files/synthbuster.zip>). Generation parameters and image resolutions follow the defaults in each repository, as listed in Table B.
- **SD3.5 and Flux-1-dev:** In the VAE category for Q2, three generators already exist in Synthbuster. We generate additional large-scale test sets from SD3.5 and Flux-1-dev, with 10,000 fake images each. Prompts are short descriptions generated by an LLM. Since corresponding real images are not available, we use the full PASCAL VOC training split, which contains 9,600 real images to compute balanced accuracy for the binary classes.
- **Satellite testing set (Q4):** The real images comprise all images from four categories of the fMoW validation set (<https://github.com/fMoW/dataset>): amusement park (2,556 images), car dealership (2,156 images), electric substation (2,626 images), and stadium (2,575 images). Each real image has associated metadata including location (country). Fake images are generated using prompts of the form: “a fMoW satellite image of {class_name} in {country}”. The number of generated images matches the number of real images for each class.